ARTICLE IN PRESS

Low ^{3}He/^{4}He ratios in basalt glasses from the western Southwest Indian Ridge (10°-24°E)

Jennifer E. Georgen [a,*], Mark D. Kurz [b], Henry J.B. Dick [c], Jian Lin [c]

[a] MIT–WHOI Joint Program in Oceanography, Woods Hole Oceanographic Institution, Woods Hole, MA 02543, USA
[b] Department of Marine Chemistry and Geochemistry, Woods Hole Oceanographic Institution, Woods Hole, MA 02543, USA
[c] Department of Geology and Geophysics, Woods Hole Oceanographic Institution, Woods Hole, MA 02543, USA

Abstract

^{3}He/^{4}He ratios and total helium concentrations have been measured in a suite of basalt glasses from the ultra-slow spreading (0.8 cm/yr half-rate) western Southwest Indian Ridge (SWIR). The study area is divided into two subregions, a supersegment between 9° and 16°E, where poorly defined ridge segments lie at a highly oblique angle to the regional spreading direction, and a supersegment between 16° and 24°E, where ridge segments are nearly orthogonal to the spreading direction. Although earlier geochemical studies suggested that the western oblique supersegment may be affected by the Bouvet plume more than 700 km to the west, there is no evidence for elevated ^{3}He/^{4}He in the region. In fact, ^{3}He/^{4}He throughout the entire study area ranges from 6.3 to 7.3 R_a, significantly below normal mid-ocean ridge basalt helium isotopic ratios of 8 ± 1 R_a. The preferred explanation for low ^{3}He/^{4}He ratios is recycled crustal or lithospheric material in the SWIR mantle source, although thorough evaluation of this explanation awaits additional geochemical data. ^{4}He concentrations for the oblique supersegment are generally lower than those for the orthogonal supersegment, which may reflect variable extents of magmatic degassing along the ridge. The low ^{3}He/^{4}He ratios are not attributable to radiogenic ingrowth following post-eruptive degassing, because ^{4}He concentrations are too high (> 0.4 μccSTP/g). In addition to low ratios, ^{3}He/^{4}He measurements for the western SWIR are characterized by low variability, which contradicts predictions of an inverse relationship between spreading rate and helium isotope standard deviation. ^{3}He/^{4}He ratios for the orthogonal supersegment increase systematically from west to east, and are positively correlated with mantle Bouguer anomaly, a correlation which is opposite to that observed in other ridge environments. Overall, the range in ^{3}He/^{4}He isotopic values for the SWIR is significantly different from that measured along other ridges, suggesting that there may be systematic variability of ^{3}He/^{4}He ratios between ridge systems.
© 2002 Published by Elsevier Science B.V.

Keywords: Helium isotopes; Southwest Indian Ridge; Bouvet plume; geochemistry

* Corresponding author. Present address: Graduate School of Oceanography, University of Rhode Island, 232 Horn Laboratory, South Ferry Road, Narragansett, RI 02882, USA. Tel.: +1-401-874-6684; Fax: +1-401-874-6811.
E-mail addresses: jgeorgen@gsosun1.gso.uri.edu (J.E. Georgen), mkurz@whoi.edu (M.D. Kurz), hdick@whoi.edu (H.J.B. Dick), jlin@whoi.edu (J. Lin).

1. Introduction

Along the global mid-ocean ridge system, areas affected by hotspots often have distinct geochemistry from 'normal' mid-ocean ridge basalt (MORB). Analyses of major element, rare earth element, and isotopic data for axial dredge samples can be merged with geophysical data such as bathymetry and gravity to delineate portions of ridge influenced by a nearby mantle plume [1–4]. Helium isotopic data are often a sensitive indicator of plume influence [5–7]. One assumption commonly made in interpreting noble gas data is that the hotspot source is relatively undegassed lower mantle. Under this assumption, high ^{3}He/^{4}He indicates plume-like upwelling, since the deep Earth is believed to be a source of primordial ^{3}He with a relatively low time-integrated (U+Th)/He ratio.

Values of ^{3}He/^{4}He for normal MORB (N-MORB) generally fall in the range of 8 ± 1, normalized to the atmospheric ratio of 1.384×10^{-6} (R_a) [9]. The assumption of a N-MORB value of 8 ± 1 R_a is based on along-axis studies (e.g. [5,10,11]) which omit significant ^{3}He/^{4}He variations near hotspots. More recent studies, incorporating data from a variety of geologic settings including ridges, back-arc basins, hotspot-influenced sections of ridge, and near-ridge seamounts, have questioned this value and suggest that the global mean ^{3}He/^{4}He ratio is 9.1 ± 3.5 R_a [12,13]. This estimate, however, suffers from numerous statistical effects, including the assumption that ^{3}He/^{4}He ratios are Gaussian-distributed and artifacts from spatial averaging of unevenly distributed data. This study makes use of MORB ratios of 8 ± 1 R_a as a benchmark [9]. However, the data presented here have implications for the definition of global average ^{3}He/^{4}He MORB values, particularly for the Southwest Indian Ridge (SWIR), because they are significantly below the putative 'normal' values.

Helium ratios around hotspots are often significantly different from those for N-MORB. For example, Hawaii has elevated ^{3}He/^{4}He, in the range of 8–32 R_a (e.g. [14–16]). In the vicinity of Iceland, ^{3}He/^{4}He increases from < 8 R_a south of the Gibbs Fracture Zone to ~ 15 R_a on the southern submarine portion of the Iceland plateau, to a high of 37 R_a on the island itself [17]. ^{3}He/^{4}He ratios in lavas from the Galapagos islands vary between 8.6 and 27 R_a (e.g. [10,18]). Moreover, Reunion Island helium measurements range from 11 to 14 R_a [19,20], and isotopic ratios for the SWIR near the Bouvet plume in the southern Atlantic Ocean reach 14.2 R_a [21].

There are also ocean islands and ridge segments with ^{3}He/^{4}He ratios lower than 8 R_a. Notably, most ^{3}He/^{4}He ratios along the Mid-Atlantic Ridge (MAR) near the Azores are as low as 7 R_a [5]. Graham et al. [22,23] found ratios along the southern MAR near Tristan da Cunha, Gough, and St. Helena to be uniformly less than 7 R_a. Possible explanations for low ^{3}He/^{4}He ratios include the addition of low He/(U+Th) material into the mantle source by recycling of subducted oceanic crust or delaminated continental lithosphere, and magma chamber or post-eruptive degassing followed by radiogenic ingrowth [5,24,25].

The goal of this investigation is to explore ^{3}He/^{4}He ratios along the western SWIR, between 10° and 24°E. This study area includes the slowest spreading rates for which ^{3}He/^{4}He ratios have yet been measured, as well as a section of ridge postulated to be affected by the Bouvet plume [26]. Surprisingly, for this ~ 800 km long portion of the SWIR, we report ^{3}He/^{4}He ratios that are both remarkably uniform and consistently below N-MORB values.

2. Geological and geochemical setting

2.1. Ridge geometry

The SWIR extends ~ 8000 km, from the Bouvet Triple Junction (BTJ) in the west to the Rodrigues Triple Junction in the east. Spreading rates along the SWIR are ultra-slow and relatively uniform, with half-rates ranging from 0.7 to 0.9 cm/yr. Two near-ridge hotspots, Bouvet and Marion, affect accretionary processes along the SWIR [27–30]. The Bouvet hotspot is located approximately 300 km east of the BTJ and ~ 50 km from the nearest spreading segment of the
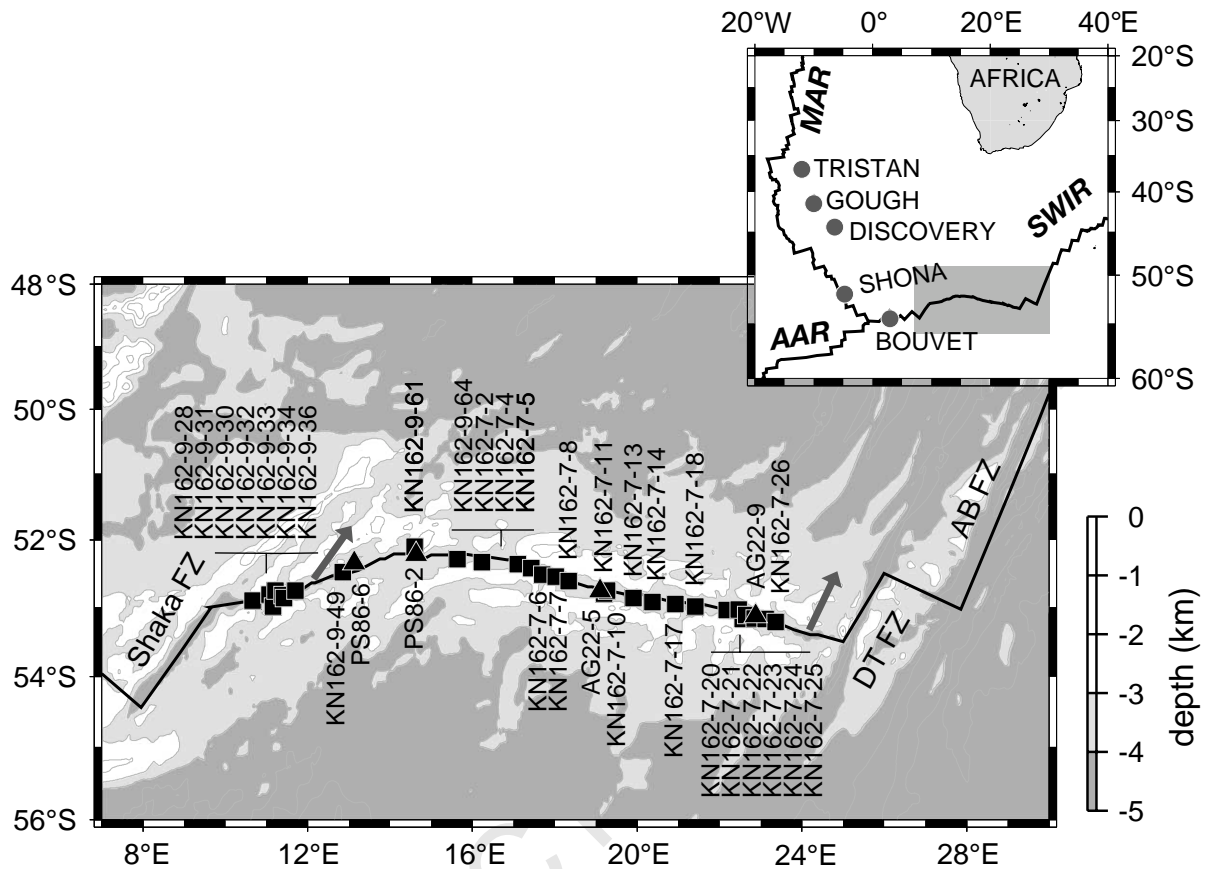
1 Fig. 1. Locations of the dredged samples analyzed in this study. Most samples are from *Knorr* cruise 162, legs 7 and 9 (KN162-
2 designation, squares); samples with PS86- and AG22-prefixes (triangles) were obtained during Leg ANT IV/4 of the F.S. *Polar-*
3 *stern* (1986) and *Agulhas* Leg 22 (1981), respectively. Arrows indicate plate spreading direction [71-72]. The ridge axis between 9°
4 and 16°E is referred to as the oblique supersegment because the ridge lies at a high angle to the regional spreading direction. In
5 contrast, spreading is nearly perpendicular to the strike of the ridge between 16° and 25°E, referred to as the orthogonal super-
6 segment. Ridge coordinates for the orthogonal supersegment are from Grindlay et al. [31]. Bathymetry data are extracted from
7 the global predicted seafloor topography database [48]. The shallowest seafloor (shaded white) is <3 km deep; the contour inter-
8 val is 1 km. DT FZ and AB FZ are the Du Toit and Andrew Bain fracture zones, respectively. Inset shows the regional setting
9 of the study area, just to the east of the Bouvet Triple Junction at ~0°E. The Bouvet Triple Junction joins the Southwest Indian
10 Ridge (SWIR), American–Antarctic Ridge (AAR), and southern Mid-Atlantic Ridge (MAR). The locations of hotspots in the vi-
11 cinity of the Bouvet Triple Junction are indicated with gray filled circles.

124 SWIR. Marion is approximately 250 km south of
125 the ridge axis in the central portion of the SWIR,
126 to the east of the Andrew Bain Fracture Zone and
127 well outside of the study area.

128   The western SWIR can be divided into three
129 sections based on spreading geometry (Fig. 1).
130 Between the BTJ and the Shaka Fracture Zone,
131 well-defined short ridge segments, which are or-
132 thogonal to the regional spreading direction, are
133 offset by relatively long-lived transform faults. In

134 contrast, segmentation is poorly defined along the
135 400 km long section of ridge between 9° and 16°E.
136 This portion of the SWIR lies at a high angle to
137 the regional spreading direction, and consequently
138 is referred to here as the oblique supersegment.
139 Because of its obliquity, this SWIR section has
140 an effective spreading rate, or spreading rate mea-
141 sured orthogonal to the local ridge trend, of only
142 0.42 cm/yr. This is the slowest rate along the ac-
143 cessible portion of the global ridge system (only

the Arctic ridges are slower). Between 16° and 25°E, the SWIR is composed of a series of short ($\sim$42 km) segments separated by non-transform offsets [31]. Since ridge segments are only 10° from perpendicular to the regional spreading direction in this area, this portion of the SWIR will be referred to as the orthogonal supersegment. The orthogonal supersegment was the focus of a detailed geophysical survey by Grindlay et al. [31], while the recent R/V *Knorr* cruise 162 (Austral summer 2000–2001) surveyed bathymetry, magnetics, and gravity of the oblique supersegment and dredged >60 locations on both the oblique and orthogonal supersegments [32].

The BTJ is the intersection of the SWIR, American–Antarctic Ridge (AAR), and MAR. Over the past few million years, half-spreading rates for the AAR and MAR have been 0.9 and 1.4 cm/yr, respectively [33]. Spiess Seamount, a large volcanic edifice on the first SWIR segment to the east of the BTJ, may reflect recent reorganization of the triple junction and/or the present-day location of the Bouvet plume [29,33].

2.2. Geochemistry: BTJ vicinity and western SWIR

Values of $^3He/^4He$ in the immediate vicinity of the BTJ range from 6.5 to 14.2 R_a [21]. Along the SWIR, relatively high (9.98–12.9 R_a) values were obtained for four samples on the ridge segment closest to the Bouvet plume; a single measurement for Bouvet Island itself is 12.4 R_a [21]. Ratios for the segments flanking the Bouvet Ridge segment are relatively low (7.12–7.45 R_a); these ratios were attributed to ambient mantle $^3He/^4He$ values lower than the global average of 8 R_a [21]. Surprisingly, however, the highest measurements were obtained for the ridge segment between the Islas Orcadas and Shaka fracture zones, where a single dredge haul included rocks with ratios ranging from 7.41 to 14.9 R_a [21]. Along the eastern AAR, $^3He/^4He$ ratios are systematically higher near the BTJ (8.95–9.71 R_a), compared to lower values between 15° and 18°W (6.68–8.1 R_a) [21].

Four hotspots are located within 750 km of the southern MAR, Tristan, Gough, Discovery, and Shona (Fig. 1). As noted previously, Tristan and Gough are both low $^3He/^4He$ hotspots, with ratios <7 R_a [22,23]. However, both Shona and Discovery are characterized by well-defined axial $^3He/^4He$ highs, with maximum $^3He/^4He$ ratios of 14.7 and 14.2 R_a, respectively [7,21,25]. To the south of Shona, in the immediate vicinity of the BTJ, $^3He/^4He$ ratios of the MAR samples return to lower values of 7.11–7.66 R_a [21]. Note that these values are slightly lower than 8 R_a, the typical value for N-MORB.

Between the BTJ and 11°E along the SWIR, normal, transitional, and enriched MORB are juxtaposed with no clear gradient away from the Bouvet plume [34]. This geochemical variability is attributed to the ultra-slow spreading rate, which allows the persistence of small, localized plume-related heterogeneities without magma mixing or homogenization [26,34]. For the oblique supersegment, isotopic, major element, and trace element data are available for six dredge hauls collected prior to the KN162 cruises [26]. Dredged lavas are highly K-enriched, nepheline-normative alkali basalts and hawaiites with highly fractionated incompatible element ratios and enriched isotopic ratios. Le Roex et al. [26] explain these basalts as the products of extremely low percentage melting ($<5\%$) of a veined mantle source. They postulate that the isotopically and trace-element-enriched veins result from lateral dispersion of the Bouvet plume more than 700 km away. A lack of published geochemical data for the orthogonal supersegment complicates evaluation of Bouvet contributions. However, several isotopic analyses of basalts from this region suggest that it is composed of isotopically depleted N-MORB [35]. Likewise, preliminary major element analysis of the same basalts used in this study suggests that the orthogonal supersegment erupts N-MORB [36].

2.3. Study motivation

This study documents variations in $^3He/^4He$ ratios along the western SWIR. Since these $^3He/^4He$ measurements correspond to the slowest spreading rates for which helium data are currently available, we first compare $^3He/^4He$ values from

Table 1
Helium data for the western SWIR, oblique supersegment (10°–16°E)

Sample	Lat. (°S)	Long. (°E)	^{4}He conc. (μccSTP/g)	^{3}He/^{4}He (R/R_a)	±	Depth (m)	Method[a]
KN162-9-28-32	−52.90	10.67	0.0184	5.81	0.26	3803	1
			0.02096	3.76	0.16	3803	3
KN162-9-31-1	**−52.81**	**11.08**	**2.02**	**6.61**	**0.05**	**3074**	**1**
			0.01842	5.94	0.20	3074	3
KN162-9-30-12	**−52.99**	**11.16**	**2.97**	**6.49**	**0.04**	**3587**	**1**
			0.05126	6.11	0.10	3587	3
KN162-9-32-11	−52.75	11.22	0.00383	4.71	1.15	2720	1
			0.003793	5.94	1.28	2720	3
KN162-9-33-51	−52.82	11.39	0.0299	1.25	0.14	1462	1
			0.003740	0.77	1.35	1462	3
KN162-9-34-39	**−52.86**	**11.43**	**2.05**	**6.52**	**0.04**	**2126**	**1**
			0.07783	6.17	0.08	2126	3
KN162-9-36-27	−52.75	11.71	13.8	6.94	0.05	4017	1
KN162-9-49-13	**−52.48**	**12.86**	**1.55**	**6.80**	**0.04**	**4193**	**1**
			0.2274	6.70	0.07	4193	3
PS86-6-1	−52.35	13.13	0.0171	3.43	0.16	4000	2
PS86-6-2	−52.35	13.13	0.02819	3.21	0.07	4000	2
			0.00242	5.98	0.40	4000	1
			0.0227	3.05	0.05	4000	3
KN162-9-61-71	−52.10	14.60	0.01391	1.18	0.08	2282	1
			0.007611	0.35	0.11	2282	3
PS86-2-14	**−52.22**	**14.63**	**15.92**	**6.26**	**0.02**	**3200**	**2**
KN162-9-64-1	−52.29	15.64	0.006447	6.31	0.34	2947	1
			0.01321	6.40	0.21	2947	3

[a] 1 = Crushing in vacuo, 2 = melting in vacuo, 3 = melting of powder produced by crushing. Bold entries have ^{4}He concentrations greater than the threshold value of 0.4 μccSTP/g. Depths for PS- and AG-cruises are approximate.

the oblique and orthogonal supersegments to measurements at faster spreading ridges. Second, we evaluate whether ^{3}He/^{4}He measurements differ systematically between the orthogonal and oblique supersegments, as a function of both proximity to the Bouvet hotspot and change in effective spreading rate. Third, we place the variability of ^{3}He/^{4}He along the western SWIR in a global context. Of particular interest is an evaluation of the hypothesis that ^{3}He/^{4}He variability for this ultra-slow spreading ridge should be high, given the linear relationship between reciprocal spreading rate and ^{3}He/^{4}He variance proposed by Allègre et al. [37].

3. Samples and analytical procedures

The samples described here primarily came from dredge sampling of the SWIR between 10° and 24°E during R/V *Knorr* legs 162-7 and 162-9 (Austral summer 2000–2001) [38]. Samples from Leg ANT IV/4 of F.S. *Polarstern* (1986) and the 1981 *Agulhas* Leg 22 cruise supplemented the *Knorr* dredges. KN162 recovered over 60 dredges along the SWIR axis, and the rocks varied in lithology and degree of alteration. The samples used in this investigation were selected for the availability of fresh basaltic glass. Vesicularities of the measured glasses range from < 1% to 5%. In general, glasses from the oblique supersegment had more iron–manganese coatings, thinner glassy rims, and higher vesicularity than glasses from the orthogonal supersegment [38]. The locations of the analyzed basalts are indicated in Fig. 1 and Tables 1 and 2.

Fresh, completely vitreous glasses in the 0.5–2 mm size fraction were handpicked under magnification and cleaned ultrasonically in ethanol and acetone. The small size of these glass chips was

Table 2
Helium data for the western SWIR, orthogonal supersegment (16°–24°E)

Sample	Lat. (°S)	Long. (°E)	^{4}He conc. (μccSTP/g)	^{3}He/^{4}He (R/R_a)	±	Depth (m)	Method[a]
KN162-7-2-1	**−52.33**	**16.23**	**0.6343**	**6.77**	**0.04**	**3855**	**1**
			0.4843	**6.58**	**0.03**	**3855**	**3**
KN162-7-4-31	**−52.36**	**17.11**	**2.972**	**6.67**	**0.03**	**3928**	**1**
			1.276	**6.55**	**0.04**	**3928**	**3**
KN162-7-5-1	**−52.42**	**17.43**	**1.106**	**6.64**	**0.04**	**3090**	1
			0.1906	6.52	0.03	3090	3
KN162-7-6-2	**−52.52**	**17.70**	**15.1**	**6.80**	**0.04**	**3582**	**1**
			10.58	**6.74**	**0.06**	**3582**	**2**
KN162-7-7-2	**−52.55**	**18.03**	**11.45**	**6.91**	**0.05**	**4001**	**1**
KN162-7-8-5	**−52.61**	**18.34**	**2.882**	**6.88**	**0.03**	**3702**	**1**
			3.679	**6.88**	**0.05**	**3702**	**3**
AG22-5-2	**−52.76**	**19.10**	**0.7269**	**6.97**	**0.03**	**3700**	**2**
AG22-5-7	**−52.76**	**19.10**	**3.541**	**7.03**	**0.06**	**3700**	**2**
AG22-5-18	**−52.76**	**19.10**	**0.717**	**6.87**	**0.03**	**3700**	**2**
AG22-5-14	−52.76	19.10	0.03521	6.67	0.10	3700	2
KN162-7-11-25	**−52.80**	**19.20**	**38.06**	**6.89**	**0.03**	**3886**	**1**
			7.449	**6.83**	**0.04**	**3886**	**3**
KN162-7-10-21	**−52.75**	**19.27**	**3.309**	**6.90**	**0.04**	**3165**	**1**
			2.787	**6.71**	**0.04**	**3165**	**3**
KN162-7-13-29	**−52.86**	**19.91**	**22.49**	**6.91**	**0.04**	**4071**	**1**
			7.144	**6.82**	**0.03**	**4071**	**3**
KN162-7-14-7	**−52.92**	**20.38**	**18.33**	**6.94**	**0.04**	**3450**	**1**
			3.820	**6.86**	**0.03**	**3450**	**3**
KN162-7-17-16	**−52.95**	**20.93**	**6.040**	**7.21**	**0.04**	**3874**	**1**
KN162-7-18-17	**−52.99**	**21.41**	**2.822**	**7.03**	**0.02**	**4507**	**1**
			10.06	**7.01**	**0.05**	**4507**	**3**
KN162-7-20-6	**−53.04**	**22.18**	**27.00**	**7.29**	**0.04**	**4246**	**1**
KN162-7-23-107	**−53.17**	**22.57**	**20.47**	**7.28**	**0.04**	**3658**	**1**
			1.626	**7.01**	**0.05**	**3658**	**3**
KN162-7-21-2	**−53.03**	**22.47**	**33.30**	**7.10**	**0.03**	**3787**	**1**
KN162-7-22-14	**−53.11**	**22.65**	**30.53**	**7.03**	**0.04**	**3875**	**1**
KN162-7-24-4	**−53.16**	**22.85**	**9.472**	**7.01**	**0.03**	**3290**	**1**
AG22-9-2	**−53.13**	**22.88**	**25.53**	**7.23**	**0.04**	**3800**	**2**
KN162-7-25-3	**−53.17**	**23.12**	**1.478**	**7.09**	**0.03**	**3995**	**1**
			12.53	**7.05**	**0.05**	**3995**	**3**
KN162-7-26-23	**−53.21**	**23.36**	**2.351**	**7.28**	**0.06**	**3325**	**1**

[a] 1 = Crushing in vacuo, 2 = melting in vacuo, 3 = melting of powder produced by crushing. Bold entries have ^{4}He concentrations greater than the threshold value of 0.4 μccSTP/g. Depths for PS- and AG-cruises are approximate.

necessary to avoid alteration. It is well known that such small grain sizes may result in loss of gas in vesicles, which should be noted when comparing helium concentrations measured in this study to those obtained elsewhere. Helium measurements were generally performed by crushing in vacuo, although a number of samples were analyzed by melting. Crushing in vacuo selectively releases helium contained by vesicles, and is the preferred method here for two reasons. First, it minimizes post-eruptive radiogenic contributions from decay of Th and U, which reside in the solid matrix. Second, based on glass–vesicle equilibrium studies, a vesicularity of 1–5% corresponds to a vesicle/glass helium concentration ratio of 1:100 (e.g. [9]). Therefore, glass matrix ^{3}He/^{4}He ratios are more susceptible to change by radiogenic ingrowth both due to higher (U+Th) and because overall gas concentrations are lower. Concentrations for most samples were determined

by both crushing and melting of the powder remaining from crushing, which then allowed estimation of total magmatic helium concentrations. All measurements were performed at Woods Hole Oceanographic Institution on a 90° sector mass spectrometer. Extraction lines for crushing and melting, mass spectrometry, and blank values are described elsewhere [16,39]. ^{4}He blanks during the course of these measurements were $\sim 6 \times 10^{-11}$ ccSTP.

Where both crushing and melting of glass chips were performed on the sample (e.g. KN162-7-6-2), the isotopic composition determined by the two methods was identical within error, which demonstrates that the ^{3}He/^{4}He ratios obtained do not reflect any crushing-induced fractionation processes. This is confirmed by step-crushing experiments performed on several samples (KN162-7-11-25, KN162-7-18-17, and KN162-9-33-49). Helium released by both lighter crushing and more extensive crushing than the normal procedure yielded identical isotopic compositions in all cases.

Complete major element, rare earth element, and isotopic data sets are not yet available for the KN162 samples. Petrographic descriptions, as well as whole rock and glass analyses for the *Polarstern* samples, can be found in le Roex et al. [26]. Isotopic, major element, and trace element data for AG22-9-2 are described in Mahoney et al. [35].

4. Results and discussion

4.1. ^{4}He concentrations

The ^{4}He concentrations and ^{3}He/^{4}He ratios (R/R_a) are reported in Tables 1 (oblique supersegment) and 2 (orthogonal supersegment). Errors for the isotopic ratios are reported as 1σ; uncertainties in the ^{4}He concentrations are typically 1–2%. Total concentrations of ^{4}He (mostly calculated as the sum of crushing plus powder melting) vary widely, from 0.0076 μccSTP/g (sample KN162-9-32-11) to 45.5 μccSTP/g (sample KN162-7-11-25); this wide variation is not unusual and indicates the important influence of degas-
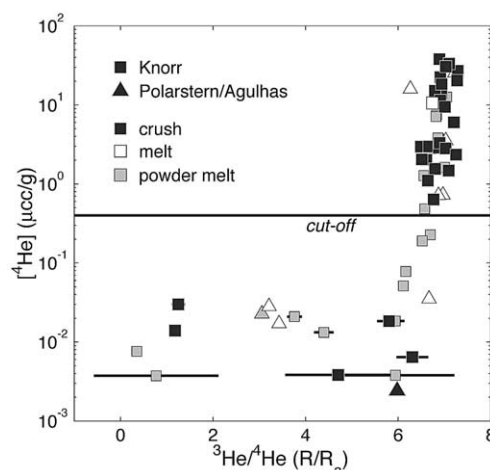
Fig. 2. Variation of ^{4}He concentration as a function of ^{3}He/^{4}He ratio. Only ^{3}He/^{4}He ratios for samples with ^{4}He concentrations above a cutoff of 0.4 μccSTP/g were considered representative of the mantle magmatic ratio, since low-^{4}He samples may have been affected by degassing and post-eruptive radiogenic ingrowth. For the remaining, high-^{4}He samples, ^{3}He/^{4}He ratios fall in the range of 6.3–7.3 R_a. The concentration threshold cutoff represented by a horizontal line at 0.4 μccSTP/g is explained in Fig. 5. All square symbols indicate glasses from KN162, while all triangle symbols represent samples from the PS86 or AG22 cruises. The shading of the symbol indicates the technique of helium measurement (black = crushing, unfilled = melting, gray = melting of the powder produced by crushing).

sing processes on the measured helium contents (Fig. 2). Wide variability of ^{4}He concentrations within a single dredge haul (e.g. AG22-5) reflects low glass availability and measurement of small glass chips (≤ 0.5 mm) for some samples (e.g. AG22-5-14).

Fig. 3 shows that ^{4}He concentrations for samples from the oblique supersegment may generally be lower than those from the orthogonal supersegment. Lower concentrations for the oblique supersegment may reflect more extensive degassing during residence in magma chambers, in transit to the surface, and/or upon eruption on the seafloor. It is noteworthy that within samples from the orthogonal supersegment, there is an apparent relationship between longitude and total helium concentration, with significantly higher ^{4}He contents farther to the east (Fig. 3). ^{4}He contents range between 0.7 and 10.58 μccSTP/g in the western orthogonal supersegment samples (16.2–
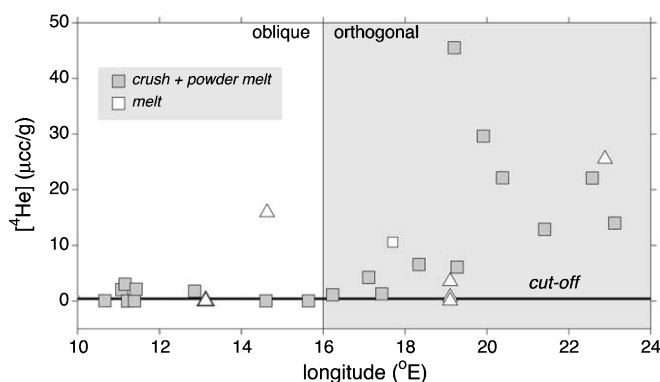
1 Fig. 3. Variation of total glass ^{4}He concentration as a function of longitude. Samples from the oblique supersegment and the
2 western orthogonal supersegment have significantly lower total ^{4}He concentrations. This longitudinal difference may reflect vari-
3 able degrees of magmatic degassing, or differences in mantle gas concentrations. The concentration threshold cutoff is represented
4 by a horizontal line at 0.4 μccSTP/g as explained in Fig. 5. As in Fig. 2, squares represent samples from KN162, and triangles
5 indicate samples from PS86 or AG22. Gas concentrations determined from the sum of melting and crushing are indicated with
6 gray symbol shading, while those determined via melting of chips only are indicated with unfilled symbols.

357 19.1°E) and between 6.0 and 45.5 μccSTP/g in the
358 east (19.2–23.4°E). Although shallower samples
359 are often more degassed, possibly reflecting the
360 effects of hydrostatic pressure on outgassing, there
361 is not a strong relationship between ^{4}He concen-
362 tration and dredge depth for the *Knorr* samples
363 (Fig. 4).
364   ^{3}He/^{4}He isotopic compositions of samples with
365 extremely low gas contents may have been af-
366 fected by degassing followed by post-eruptive ra-
367 diogenic ingrowth or seawater interaction. To
368 avoid overinterpretation of such data, this discus-
369 sion focuses exclusively on samples with ^{4}He con-
370 centrations greater than 0.4 μccSTP/g. Over time
371 scales of < 1 Myr, it is unlikely that post-eruptive
372 radiogenic ingrowth of ^{4}He by U+Th decay
373 would affect the ^{3}He/^{4}He ratios of samples with
374 concentrations higher than this. After 1 Myr of
375 radiogenic ingrowth in a closed system, a sample
376 with a ^{4}He concentration of 0.4 μccSTP/g and an
377 initial ^{3}He/^{4}He ratio of 8 R_a would decrease by
378 only 10% (Fig. 5), assuming a uranium concentra-
379 tion [U] of 0.6 ppm [21] and a Th/U ratio of 3
380 [40]. Although Th data are not yet available for
381 the study area, the mean dredge-averaged [U] for
382 the orthogonal supersegment is 0.11 ppm
383 (range = 0.04–0.22 ppm), and for the oblique
384 supersegment is 0.5 ppm (range = 0.06–1.60 ppm)
385 (Standish et al., in preparation). The assumption

386 of a relatively high [U] concentration of 0.6 ppm,
387 therefore, yields an upper bound on ^{3}He/^{4}He ratio
388 decrease due to radiogenic ingrowth.
389   A decrease in ^{3}He/^{4}He ratio of 10% is a signifi-
390 cant threshold because the highest ^{3}He/^{4}He ratio
391 among the samples was 7.29 R_a, approximately
392 10% below the N-MORB reference of 8 R_a.
393 Moreover, ∼ 10 Myr would be required for the
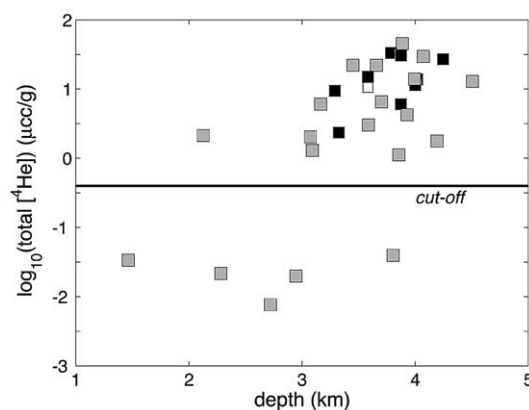394 ^{3}He/^{4}He ratio for a sample with ^{4}He = 4 μccSTP/g

Fig. 4. Concentration of ^{4}He as a function of seafloor depth
for the *Knorr* samples. ^{4}He concentrations for the *Polarstern*
and *Agulhas* samples were not plotted because depths for
these samples are poorly constrained. Symbols are as in Fig.
2. The concentration threshold cutoff represented by a hori-
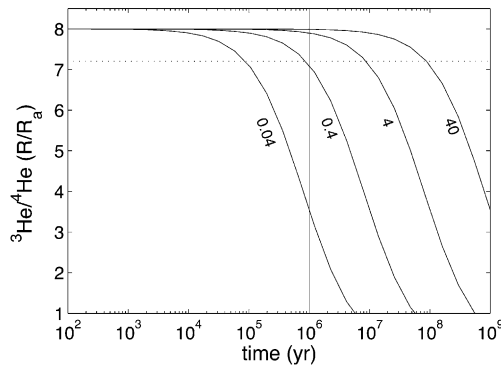zontal line at 0.4 μccSTP/g is explained in Fig. 5.

Fig. 5. Predicted time-dependent evolution of $^3He/^4He$ ratios resulting from post-eruptive radiogenic ingrowth of ^4He by decay of U+Th. Curves were calculated for four initial ^4He concentrations, 0.04, 0.4, 4, and 40 μccSTP/g, overlapping the concentration range observed in the SWIR sample suite. Assumptions include an initial $^3He/^4He$ ratio of 8 R_a, [U] of 0.6 ppm [21], and a Th/U ratio of 3 [40]. Dashed line indicates 10% reduction in initial $^3He/^4He$ ratio. This study interprets only samples with concentrations sufficiently high that post-eruptive radiogenic ingrowth does not lower their $^3He/^4He$ ratio below the 10% threshold for time scales <1 Myr. This concentration threshold corresponds to 0.4 μccSTP/g, and is indicated in Figs. 2–4.

to decrease by 10%. For $^4He = 40$ μccSTP/g, approximately the highest concentration measured in this suite of basalts, this time scale is on the order of 100 Myr. In 1 Myr, the decrease in $^3He/^4He$ for $^4He = 40$ μccSTP/g is smaller than analytical error. Therefore, a concentration cutoff of 0.4 μccSTP/g is very conservative both because the samples were dredged at the ridge axis and are most likely ≪1 Myr in age, and also because

these calculations assume fairly high Th+U concentrations.

4.2. Eruption ages

Helium isotope disequilibrium between vesicles and glass can be used to constrain the maximum eruption age of seafloor samples [21,41], a parameter that is of considerable interest in this ultra-slow spreading environment. Because the (U+Th)/He method of dating is most successful for samples with low gas concentrations [41], we focus on glasses with melting-derived [^4He] below the concentration cutoff. We also calculate ages only for those samples for which $^3He/^4He_{crush}$ differs from $^3He/^4He_{powder_{melt}}$ by more than 2σ. Additionally, we assume that [U] = 0.6 ppm [21], Th/U = 3 [40], helium was in equilibrium at eruption, and the only source of low $^3He/^4He$ ratios is radiogenic ingrowth. All samples that meet these requirements are from the oblique supersegment. As discussed above, the assumption of a uranium concentration of 0.6 ppm is close to the mean [U] of 0.5 ppm along the oblique supersegment, and falls within the measured range of 0.06–1.60 ppm (Standish et al., in preparation).

One set of model calculations assumes that initial isotopic compositions are equal to the $^3He/^4He$ ratios obtained by crushing. The resultant eruption ages range from 15 to 90 kyr (Table 3). In a second set of calculations, where the initial composition is set equal to the highest $^3He/^4He$ ratio obtained in the survey area (7.29 R_a), the

Table 3
Eruption ages

Sample	Crushing		Melting[a]		Age 1[b]	Age 2[b]
	^4He conc. (μccSTP/g)	$^3He/^4He$ (R/R_a)	^4He conc. (μccSTP/g)	$^3He/^4He$ (R/R_a)	(kyr)	(kyr)
KN162-9-28-32	0.0184	5.81	0.02096	3.76	60	82
KN162-9-31-1	2.02	6.61	0.01842	5.94	15	28
KN162-9-30-12	2.97	6.49	0.05126	6.11	24	67
KN162-9-34-39	2.05	6.52	0.07783	6.17	34	96
PS86-6-2	0.00242	5.98	0.0227	3.05	90	107
KN162-9-61-71	0.01391	1.18	0.007611	0.35	43	59

[a] Reported values correspond to melting of the powder produced by crushing.

[b] Age 1 was calculated by assuming that the initial isotopic composition was equal to the composition provided by crushing. Age 2 sets the initial composition to the highest $^3He/^4He$ ratio in the survey area, 7.29 R/R_a.
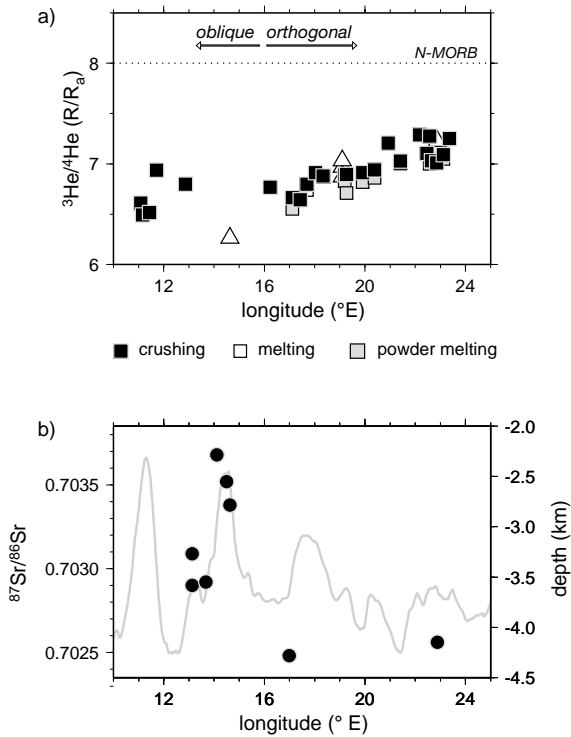
1 Fig. 6. (a) ^{3}He/^{4}He ratios along the SWIR between 10° and
2 24°E. Horizontal line at 8 R_a indicates average ^{3}He/^{4}He for
3 normal mid-ocean ridge basalt (N-MORB). As in Fig. 2,
4 symbol shape indicates cruise (squares = KN162, trian-
5 gles = PS86 or AG22) and symbol color indicates helium
6 analysis technique (black = crushing, unfilled = melting,
7 gray = melting of the powder produced by crushing). (b) ^{87}Sr/
8 ^{86}Sr ratios along the oblique and orthogonal supersegments.
9 Data are from le Roex et al. [26] and Mahoney et al. [35].
10 Gray line shows axial topography, extracted from the pre-
11 dicted topography database [48].

435 calculated eruption ages are slightly older, ranging
436 from 28 to 107 kyr.

437 These calculations indicate that ^{3}He/^{4}He ratios
438 for low-^{4}He samples can be significantly altered
439 by post-eruptive radiogenic ingrowth on ∼100
440 kyr time scales, and demonstrate the necessity of
441 making measurements by crushing in vacuo and
442 using a cutoff concentration. It should be clearly
443 noted, however, that the complete suite of U and
444 Th measurements is not yet available for these
445 samples, and therefore these age calculations are
446 only estimates. Also, in the absence of other rare
447 gas isotopic data, it is difficult to rule out contri-
448 butions by atmospheric contamination, as is sug-

449 gested by near-atmospheric ^{3}He/^{4}He ratios in
450 samples such as KN162-9-33-51 (1.25 R_a) and
451 KN162-9-61-71 (1.18 R_a). Nevertheless, these cal-
452 culated ages are geologically reasonable, and sug-
453 gest that Th–U–He ages will be useful for MORB
454 [21].

4.3. ^{3}He/^{4}He ratios   455

456 For samples with ^{4}He concentrations above 0.4
457 µccSTP/g, ^{3}He/^{4}He ratios vary between 6.3 and
458 7.3 R_a (Fig. 6a). These values are assumed to
459 represent the mantle and are uniformly below
460 the global average of 8 R_a for N-MORB, an ob-
461 servation that is discussed further below. ^{3}He/^{4}He
462 ratios for the oblique supersegment show no sys-
463 tematic trend with longitude, though there are
464 relatively few data points (Fig. 6a). In contrast,
465 for the eastern portion of the study area, there is a
466 trend of increasing ^{3}He/^{4}He ratios toward the Du
467 Toit Fracture Zone (Fig. 7). Isotopic ratios for
468 the samples east of 16°E are well described by a
469 linear relationship between ^{3}He/^{4}He and longi-
470 tude, with $r^2 = 0.71$. Over this region, ^{3}He/^{4}He
471 ratios increase by approximately 0.8 R_a, or
472 roughly 20 times the average 1σ measurement er-
473 ror.

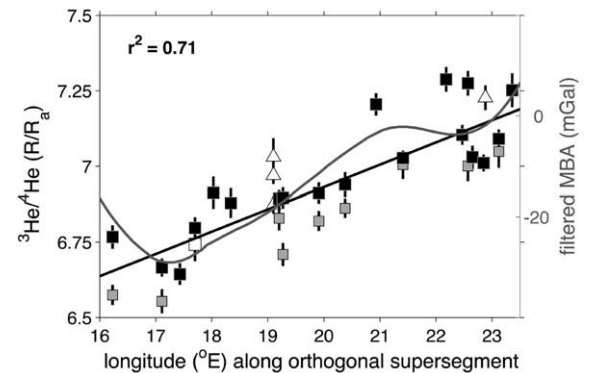1 Fig. 7. ^{3}He/^{4}He ratios increase eastward along the orthogo-
2 nal supersegment. Least-squares regression (black line) indi-
3 cates that ^{3}He/^{4}He and longitude are correlated with
4 $r^2 = 0.71$. There is also a correlation between long-wavelength
5 mantle Bouguer anomaly (MBA, gray line) and ^{3}He/^{4}He ra-
6 tios. The MBA profile was calculated by applying a 150 km
7 cutoff lowpass filter to the MBA data in Grindlay et al. [31],
8 sampled every 10 km. Symbols are the same as in Fig. 2.

As noted earlier, ^{4}He concentrations are generally lower in the western portion of the orthogonal supersegment than in the eastern portion. Interestingly, both long-wavelength mantle Bouguer anomaly (MBA, Fig. 7) and the geoid also increase from 16° to 24°E. Lower values of MBA indicate thickened crust, higher mantle temperatures, and/or lower crustal density [42,43]. A trend of eastward-increasing MBA along the orthogonal supersegment is generally consistent with the supersegment's position between the thermally warm BTJ region and the cool, long-offset Du Toit and Andrew Bain fracture zones [30]. However, a positive correlation between MBA and ^{3}He/^{4}He ratio is unusual in both hotspot-affected (e.g. Iceland) and non-hotspot-affected (e.g. Australian–Antarctic Discordance) settings, where the ^{3}He/^{4}He–MBA correlation is often negative [44,45]. Although a definitive explanation for this relationship is lacking, it is important to note that a prominent, roughly circular global geoid high, with a diameter of a few thousand kilometers, is centered at approximately the location of the Marion plume [46]. This geoid high indicates a deep-seated and spatially extensive planetary-scale density anomaly which could contribute to the gravity gradient observed for the orthogonal supersegment. In Iceland, the geoid and ^{3}He/^{4}He ratios decrease in concert away from the hotspot because both are controlled by the same plume. However, for the oblique and orthogonal supersegments, trends in the geoid may reflect long-wavelength convection processes outside the study area which are unrelated to local geochemical systematics. The positive ^{3}He/^{4}He–MBA correlation may therefore result from local ^{3}He/^{4}He variability superimposed on regional or planetary-scale gravity trends.

Although we do not have sufficient data to constrain the cause of the correlation between ^{4}He concentration and ^{3}He/^{4}He ratio along the orthogonal supersegment, we consider two possible explanations for the correlation. One plausible way of interpreting the low ^{4}He concentrations on the western side of the orthogonal supersegment is that basalts there have undergone more extensive degassing on the way to the surface. If that is the case, then the low glass helium concentrations are not source-related. Another plausible explanation for the low concentrations is that there was a recent mantle degassing event that lowered the ambient mantle helium concentrations, which could result in slightly lower ^{3}He/^{4}He ratios given sufficient time. For example, assuming 10% partial melting and typical U/Th ratios, the time required to significantly lower ^{3}He/^{4}He ratios would be on the order of 5–10 Myr. This would assume that the measured glass concentrations reflect actual mantle gas contents, unaffected by degassing in magma chambers or during eruption, or degree of partial melting. One mechanism that could result in mantle degassing is a past partial melting event. We speculate that the orthogonal supersegment's proximity to the BTJ may result in inheritance of mantle previously melted at the MAR and AAR.

4.4. ^{3}He/^{4}He variability and spreading rate

Because the SWIR samples were dredged from a portion of ridge with extremely slow spreading rate, it is important to compare their ^{3}He/^{4}He ratios to those obtained for samples from faster-spreading ridges. We compiled all available ^{3}He/^{4}He measurements for ultra-slow spreading SWIR, slow spreading MAR, and intermediate spreading Southeast Indian Ridge (SEIR) glasses from the RIDGE PETDB database [47], and supplemented this compilation with new analyses for the SEIR by Graham et al. [45]. Samples that occur within a plume-affected region were removed from the data set. We define plume-affected regions as areas with seafloor $> \sim 20\%$ shallower or deeper than a local baseline depth, following the methods of Ito and Lin [4] and using ridge topography profiles from [4,8,23,30,48–50]. We also eliminate measurements from the Australian–Antarctic Discordance (AAD) along the SEIR, an area with unusually cool mantle temperatures.

Examining similarly filtered data sets from the MAR, SWIR, Central Indian Ridge, Juan de Fuca Ridge, and East Pacific Rise, Allègre et al. [37] suggested a linear correlation between ^{3}He/^{4}He standard deviation and reciprocal spreading rate. Fig. 8 shows the correlation suggested by

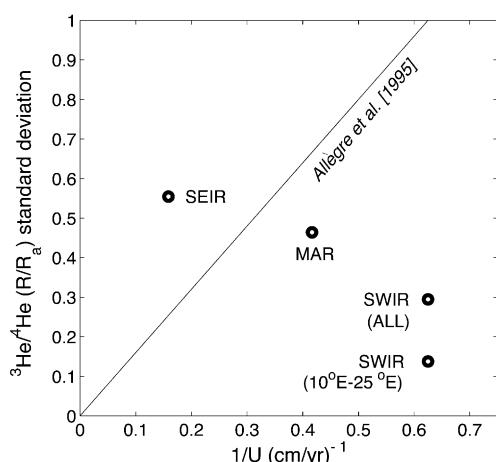1   Fig. 8. Standard deviation of $^3He/^4He$ ratios measured on
2   MORB glasses as a function of inverse spreading rate for
3   the Mid-Atlantic Ridge (MAR), Southeast Indian Ridge
4   (SEIR), and Southwest Indian Ridge (SWIR). To calculate
5   $^3He/^4He$ variability, we first eliminated all samples lying
6   within a plume-affected region. Plume-influenced regions
7   were defined by axial depth anomalies following Ito and Lin
8   [4]. Data from the Australian–Antarctic Discordance along
9   the SEIR, a region with unusually cool mantle temperatures
10   [65-66], were also eliminated. For each ridge, standard devia-
11   tion was then calculated using all of the remaining samples
12   after removing linear trends from the data. The relationship
13   suggested by Allègre et al. [37], correlating high $^3He/^4He$ ra-
14   tio standard deviation with slow spreading rate, is shown
15   with a black line. The points for the SEIR ($n = 85$), MAR
16   ($n = 93$), and SWIR (all, $n = 44$), which reflect the improved
17   global data set since 1995, do not strongly support such a
18   correlation. Notably, the standard deviation for samples
19   from 10° to 25°E along the SWIR is considerably lower than
20   that for the MAR, SEIR, or total SWIR data sets.

568   Allègre et al. [37], with respect to the new SWIR
569   data reported here. These data and the recent
570   MAR and SEIR databases do not support a pos-
571   itive correlation between $^3He/^4He$ and spreading
572   rate. However, it is clear from Fig. 8 that the
573   samples from 10° to 24°E on the SWIR have sig-
574   nificantly lower standard deviation than the
575   MAR, SEIR, or full SWIR data sets. This relative
576   uniformity in helium isotopic ratios is in strong
577   contrast to the variability along the SWIR be-
578   tween the BTJ and 7°E, where ratios range from
579   7.12 to 14.9 R_a, as well as to the heterogeneity of
580   other isotopic systems, such as $^{87}Sr/^{86}Sr$ ratios
581   [26], discussed next.

4.5. Influence of the Bouvet plume on $^3He/^4He$ ratios

582
583

Based primarily on similarities between the Sr–
Nd–Pb isotopic compositions of dredged glasses
from 10° to 13°W and those from near Bouvet
Island, le Roex et al. [26] suggested that the man-
tle beneath the oblique supersegment has been
influenced by the Bouvet plume. Although the
data are sparse, Fig. 6 shows that $^{87}Sr/^{86}Sr$ ratios
of the oblique supersegment (0.7029–0.7036) are
significantly higher than those of the orthogonal
supersegment (~ 0.7025). Despite this and other
geochemical evidence for influence of the Bouvet
plume on the oblique supersegment [26], helium
isotopes do not indicate that a deep-seated, rela-
tively undegassed mantle plume is presently affect-
ing accretionary processes along this portion of
the SWIR. Over the oblique supersegment, $^3He/$
^4He ratios range from 6.26 to 6.94 R_a, signifi-
cantly below values for N-MORB. Since Bouvet
is a 'high $^3He/^4He$' hotspot (with ratios up to 13
R_a), these values do not suggest mixing between a
source with N-MORB $^3He/^4He$ ratios and a Bou-
vet plume end-member (Fig. 9). We explore three
possible explanations for the apparent discrep-
ancy between helium isotopes and other geochem-
ical data. The first explanation involves spatial
decoupling between helium and other isotopic sys-
tems in a broadly distributed Bouvet plume. The
second explanation invokes distribution of dis-
crete, enriched domains derived from a smaller
Bouvet plume along the SWIR and AAR. The
third, preferred explanation suggests that the
low $^3He/^4He$ ratios are characteristic of a widely
distributed, heterogeneous South Atlantic mantle
source that does not necessarily require the in-
volvement of the Bouvet plume.

582
583
584
585
586
587
588
589
590
591
592
593
594
595
596
597
598
599
600
601
602
603
604
605
606
607
608
609
610
611
612
613
614
615
616
617
618

4.5.1. Broad Bouvet plume

The first explanation posits that lateral disper-
sion of the Bouvet plume away from its vertically
upwelling plume conduit at Bouvet Island (3°E) is
broad. Absolute plate motion of the African and
Antarctic plates would shear upwelling plume ma-
terial to the east [51], similar to the case of the
Galapagos plume [18]. For Galapagos, Kurz and
Geist [18] postulate that helium is preferentially

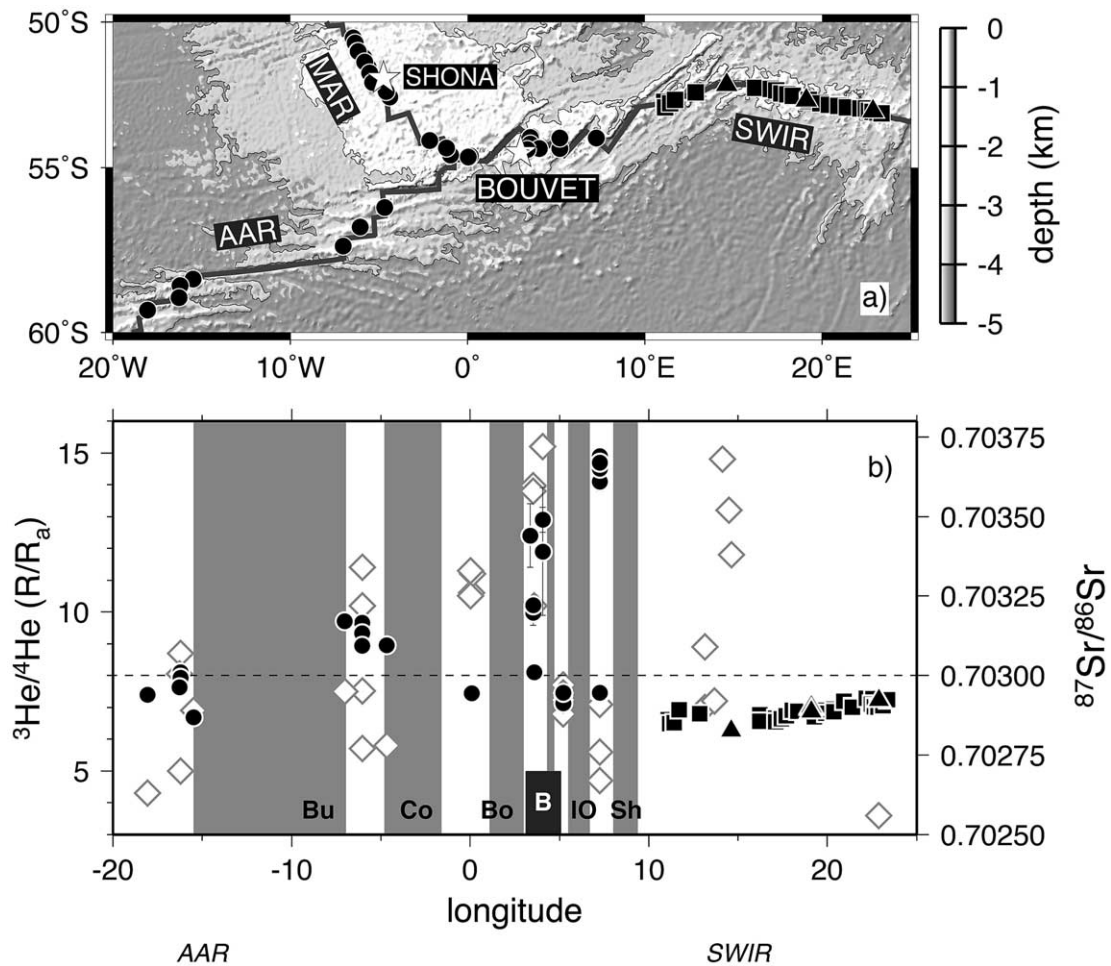619
620
621
622
623
624
625
626
627

Fig. 9. (a) Map of predicted seafloor topography in the Bouvet Triple Junction region (data from [48]), showing the locations of [3]He/[4]He measurements (squares are *Knorr* samples, triangles are *Polarstern/Agulhas* samples, and circles are from [21] or [7]). AAR = American–Antarctic Ridge, MAR = Mid-Atlantic Ridge, and SWIR = Southwest Indian Ridge. White stars give the positions of the Bouvet and Shona hotspots. Contour lines indicate 3 and 4 km depth, and an artificial illumination is imposed from the NW. (b) [3]He/[4]He (filled symbols) and [87]Sr/[86]Sr (diamonds) data along the AAR and SWIR. The names of selected fracture zones are labeled as Bu = Bullard FZ, Co = Conrad FZ, Bo = Bouvet FZ, IO = Islas Orcadas FZ, and Sh = Shaka FZ. Rectangle marked with a 'B' indicates the interpreted position of the Bouvet plume. Dashed line at 8 R/R_a indicates N-MORB [3]He/[4]He reference level. Data are from le Roex et al. [26], Mahoney et al. [35], and Kurz et al. [21].

extracted from the vertically upwelling plume, resulting in [3]He/[4]He values that are high at Fernandina, inferred to be directly over the plume conduit, and that decrease rapidly away from the plume center. In contrast, plume-like isotopic ratios of Sr, Nd, and Pb, elements assumed to be less incompatible than He, remain in the advected plume mantle farther away from the center of focused upwelling. By analogy, samples dredged far from the Bouvet conduit, but still within the range of Bouvet influence, could have low [3]He/[4]He ratios but enrichments in other isotopic systems. In this way, the oblique supersegment could be influenced by Bouvet but lack high [3]He/[4]He ratios.

Geophysical evidence strongly argues against the broad Bouvet plume hypothesis. For example, integrated analysis of gravity and bathymetry

data indicates that the Bouvet plume along-axis anomaly is strongly localized between the Bouvet and Islas Orcadas fracture zones, ∼ 300 km from the oblique supersegment [30]. Moreover, although a broad thermal plume should be associated with thickened crust (e.g. [52]), crustal thickness for the oblique segment is likely to be significantly less than that of normal oceanic crust, as inferred from gravity analysis [53] and extensive recovery of peridotite over large regions of the seafloor [32]. Also, we have already noted that major element, trace element, and other isotopic data suggest that the Bouvet plume influence can be traced along the SWIR more than 700 km eastward from the inferred location of the upwelling plume [26]. Similar evidence exists for Bouvet plume influence along the AAR, to distances of as much as 1200 km away from the plume conduit [54]. As pointed out by le Roex et al. [54], it is unlikely that the geochemistry of approximately 2000 km of ridge is governed by direct lateral dispersion from such a diminutive plume as Bouvet. For comparison, the geochemical signature of Iceland, one of the largest plumes presently affecting the global mid-ocean ridge system [55] and significantly larger than Bouvet, is observed along approximately the same length of the MAR [56]. For these reasons, we discount invoking broad plume dispersal to explain the low ^{3}He/^{4}He values for the oblique supersegment.

4.5.2. Dispersion of enriched mantle domains from Bouvet

An alternative mechanism of Bouvet dispersion would involve upwelling plume material distributed throughout the ambient mantle in discrete enriched domains along the SWIR and AAR by long-wavelength asthenospheric flow [54]. As asthenospheric flow transports the enriched domain beneath a mid-ocean ridge, the domain melts to produce either E-, T-, or N-MORB, depending on the ratio of domain to ambient mantle that is melted. Unlike the broad plume hypothesis, this dispersion mechanism does not require an unduly large Bouvet plume flux. Le Roex et al. [26] suggest that the enriched domains are present to at least ∼ 14.5°E. Because of limited geochemical data, it is unclear how much farther east these

postulated enriched domains may extend, or whether or not there may be a gradient in domain volume from west to east. Application of geodynamic numerical modeling results of plume–ridge interactions [57,58] suggests that it is unlikely that domains from a low-flux Bouvet point source flowed more than 1500 km east to the orthogonal supersegment. Therefore, in view of the widespread nature of isotopic variability in the South Atlantic described in the following section, as compared to the more limited spatial distribution of Bouvet-related material, we next explore the notion that small-scale heterogeneity is characteristic of the South Atlantic mantle source, independent of the Bouvet plume.

4.5.3. Nature of the South Atlantic mantle source

In the immediate vicinity of Bouvet, low and high ^{3}He/^{4}He ratios are intermingled over short distance scales, in some cases within single dredges [21], suggesting melting of a heterogeneous mantle with at least two end-members, a high ^{3}He/^{4}He source and a low ^{3}He/^{4}He source. Interestingly, outside of the immediate influence of other hotspots like Shona and Discovery, low ^{3}He/^{4}He ratios are also observed throughout the South Atlantic, along the southern MAR, the AAR, and the SWIR [8,21,25]. The simplest explanation for the anomalous ratios observed in this investigation, therefore, may be that low ^{3}He/^{4}He ratios are characteristic of the entire ambient South Atlantic mantle, extending eastward to the Andrew Bain Fracture Zone complex along the SWIR. Unlike large plumes such as Iceland, the flux of the high ^{3}He/^{4}He Bouvet hotspot is insufficient to overprint the He systematics of this low ^{3}He/^{4}He mantle, and to create a coherent, long-wavelength trend of decreasing ^{3}He/^{4}He ratios away from the hotspot.

Compared to the relative uniformity of ^{3}He/^{4}He isotopes, systems such as Sr and Nd show striking variability throughout the study area (Figs. 6b and 9b). In dredges west of 16°E, ^{87}Sr/^{86}Sr ratios are variable and relatively high (0.70290–0.70368) compared to N-MORB [26]. Similarly, ^{143}Nd/^{144}Nd ratios are variable but generally range to low values (0.512837–0.513020) [26]. In contrast, east of 16°E, the few available

analyses suggest that $^{87}Sr/^{86}Sr$ ratios are low (~ 0.70250) while $^{143}Nd/^{144}Nd$ ratios are high (~ 0.51310) [35]. It would appear, therefore, that the required South Atlantic mantle source must be capable of generating a large range of Sr and Nd isotopic compositions at low degrees of melting. This variability may be explained by the presence of isotopically enriched mantle veins such as garnet pyroxenite. The relative uniformity of the isotopic composition of helium from 10° to 24°E is likely to reflect only the bulk composition of the mantle because of the rapid nature of He diffusion [59]. It is improbable that He isotopic disequilibrium between the veins and the ambient mantle could persist over mantle upwelling time scales. For example, using a diffusivity of 2×10^{-8} cm^2/s for clinopyroxene (at 1250°C; [59]), helium will diffuse almost 8 m in only 1 million years.

Pyroxenitic veins are widely distributed in small quantities ($< 1\%$) in mantle xenoliths, alpine peridotites and ophiolites, and are believed to be common in the mantle [60]. Pyroxenitic veins may also have lower melting temperature than peridotite and could melt at greater pressures (e.g. [61]). Thus, where the absolute degree of melting is low, a small percentage of mantle vein material, relatively enriched in incompatible elements compared to the surrounding mantle peridotite, can potentially dominate the melt composition. In such a case, the isotopic systematics suggest two different melting scenarios for the oblique and orthogonal supersegments. In one scenario, the vein/ambient mantle ratio remains constant, but melt percentage increases, from west to east. Hotter mantle temperatures in the east could result from higher effective spreading rates along the orthogonal supersegment than the oblique supersegment [62,63]. Thus, in the west, Nd and Sr isotopic signatures would be dominated by melting of isotopically enriched mantle veins. In the east, however, at higher degrees of melting, melt compositions would be dominated by the isotopically depleted ambient mantle source, effectively masking the signal of the volumetrically smaller veins. In the second scenario, the degree of melting remains constant and relatively low throughout the study area, but the percentage or composition of the veins changes from west to east.

However, this second scenario is inconsistent with the abundance of serpentinized peridotite and the near-absence of basaltic rocks over large regions of the seafloor along the oblique supersegment, which contrasts with the abundant basalt and scarce peridotite dredged along the orthogonal supersegment [32]. This contrast seems to require different extents of melting in the two supersegments.

As discussed in the next section, pyroxenite veins have also been proposed to explain low $^3He/^4He$ ratios observed in the Australian–Antarctic Discordance, a region of unusually low mantle temperature [45]. Although a veined mantle source could be consistent with the isotopic data currently available for the oblique and orthogonal supersegments, more thorough characterization of the South Atlantic mantle source awaits additional geochemical analyses of the basalts analyzed in this study, which will be published in a subsequent paper (Standish et al., in preparation). Accordingly, in the following section, we further speculate on the possible origin of the low $^3He/^4He$ signal.

4.6. Origin of low $^3He/^4He$ values

A salient characteristic of the oblique and orthogonal supersegments is $^3He/^4He$ ratios that are uniformly below the putative 'normal' MORB value. Fig. 10 shows $^3He/^4He$ frequency histograms for each of the ridges in Fig. 8. Compared to the MAR and SEIR, a large fraction of all non-plume-affected SWIR measurements are < 7.5 R_a (Fig. 10b). Moreover, between 10° and 24°E, all existing measurements are < 7.5 R_a. Although the previous section describes how a heterogeneous mantle source could relate to low $^3He/^4He$ ratios, several other potential causes of these low $^3He/^4He$ ratios are now evaluated.

4.6.1. Degassing

As discussed in an earlier section, degassing followed by post-eruptive radiogenic ingrowth of ^4He by decay of U+Th can lower time-integrated $^3He/^4He$ ratios. However, the use of a threshold ^4He concentration makes it unlikely that radiogenic ingrowth is sufficient to decrease SWIR
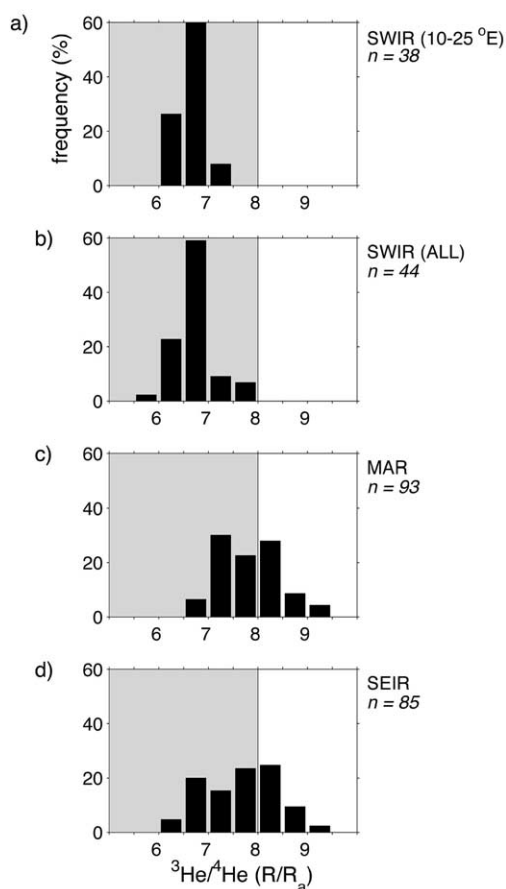
Fig. 10. Frequency histograms of ^{3}He/^{4}He ratios for non-plume-influenced MORB glasses from (a) the SWIR between 10° and 25°E, (b) the entire Southwest Indian Ridge, (c) the Mid-Atlantic Ridge, and (d) the Southeast Indian Ridge, excluding data from the Australian–Antarctic Discordance. Note that all samples available for 10–25°E SWIR have ^{3}He/^{4}He ratios below 7.5 R_a. As spreading rate increases, the peak in ^{3}He/^{4}He ratios appears to become less pronounced and may shift to higher values.

^{3}He/^{4}He ratios by approximately 1–2 R_a, from 8 R_a to 6–7 R_a. Therefore, degassing alone does not seem to explain the low ^{3}He/^{4}He ratios.

4.6.2. Preferential melting of clinopyroxene

In a study of Juan de Fuca Ridge basalts, Lupton et al. [64] explain correlations between ^{3}He/^{4}He ratios, $Na_{8.0}$, and $Fe_{8.0}$ by invoking preferential melting of clinopyroxene. They point out that most U and Th in peridotite is located in clinopyroxene, and that clinopyroxene melting contrib-

utes relatively larger proportions to melts formed at lower temperatures. Therefore, they suggest that cooler, slower-spreading ridges should systematically have lower ^{3}He/^{4}He ratios than warmer, faster-spreading ridges. Although this explanation is consistent with low ^{3}He/^{4}He ratios at the ultra-slow spreading SWIR, rapid He diffusion makes it unlikely that mineral-scale isotopic heterogeneity can persist for characteristic time scales of > 100 yr [59]. Thus, preferential melting of clinopyroxene at low mantle temperatures cannot explain low ^{3}He/^{4}He ratios.

4.6.3. Vertically stratified mantle

^{3}He/^{4}He ratios as low as 6.2 R_a have been observed for basalts from the AAD [45]. Analysis of basalts [65] and numerical modeling work [66] suggest that mantle temperatures may be as much as 150°C lower in the AAD than along surrounding sections of the SEIR. Graham et al. [45] note a correlation between ^{3}He/^{4}He ratios and $Fe_{8.0}$, implying that lower ^{3}He/^{4}He ratios are associated with shallower depths of melting. Two possible explanations for this correlation include a vertically stratified mantle and melting of discrete heterogeneities [45]. The first explanation assumes that the upper mantle is vertically stratified, with relatively more degassed material with lower ^{3}He/^{4}He ratios overlying less degassed material. Since melting occurs at shallower depths for thermally cool ridges such as the western SWIR and eastern SEIR than for faster-spreading or warmer ridges, melts produced at cool ridges should have lower ^{3}He/^{4}He ratios. A good test of this hypothesis for the SWIR will come from $Fe_{8.0}$ variation along the orthogonal and oblique supersegments, data which are not yet available. Interestingly, the portion of the SWIR between the Melville Fracture Zone at 61°E and the Rodrigues Triple Junction at 70°E has the greatest axial depth along the entirety of the SWIR, suggesting anomalously cool mantle temperatures [67,68]. However, limited investigation of ^{3}He/^{4}He ratios from the eastern SWIR near the Rodrigues Triple Junction has yielded values of 7.68, 8.11, and 8.09 R_a [69], higher than values observed along the orthogonal and oblique supersegments and counter to the predictions of the vertically stratified

890 mantle model. Furthermore, three-dimensional
891 thermal modeling calculations for passive plate
892 separation predict that for depths within the melt-
893 ing region, axial temperature for the oblique
894 supersegment is approximately 50–100°C lower
895 than the orthogonal supersegment [62]. Therefore,
896 if the vertically stratified mantle model applies,
897 there should be a systematic difference between
898 predicted, relatively low $^3He/^4He$ ratios along
899 the oblique supersegment and predicted, relatively
900 high $^3He/^4He$ ratios for the orthogonal superseg-
901 ment. Although the predicted difference between
902 oblique and orthogonal supersegment $^3He/^4He$ ra-
903 tios may not be as great as the AAD $^3He/^4He$
904 anomaly because of the overall colder thermal
905 regime of the SWIR, no such difference was ob-
906 served.

907 *4.6.4. Mantle heterogeneities*
908 Preferential melting of discrete mantle hetero-
909 geneities with lower solidus temperature than sur-
910 rounding material may also result in low $^3He/^4He$
911 ratios [45]. As described in an earlier section, for
912 example, if crustal recycling veined the AAD
913 MORB source with low-$^3He/^4He$ garnet pyroxe-
914 nite, then such veins would form a relatively large
915 proportion of melt generated at cool ridges be-
916 cause they melt preferentially to mantle peridotite
917 [45]. With increasing mantle temperature and
918 depth of melting, mantle peridotite with higher
919 $^3He/^4He$ would dilute garnet pyroxenite melts, re-
920 sulting in MORB with higher $^3He/^4He$ ratios. In
921 general, the most likely explanation for low $^3He/$
922 ^4He ratios appears to be introduction of recycled
923 crustal or oceanic lithospheric material (e.g.
924 [5,22,24,70]), with relatively high (U+Th)/He ra-
925 tios, into the source region for orthogonal and
926 oblique supersegment MORB. It is possible that
927 this recycled material is associated with the South
928 Sandwich subduction zone, which is the closest
929 subduction zone to the study area. It is important
930 to note, however, that evaluation of this hypoth-
931 esis requires geochemical data from the oblique
932 and orthogonal supersegments that are not yet
933 available.
934 Overall, the existence of low $^3He/^4He$ ratios
935 over a long portion of the SWIR suggests that
936 the average value of 8 ± 1 R_a for N-MORB may

937 need to be referenced judiciously. It is possible
938 that average MORB $^3He/^4He$ ratios vary between
939 ridge systems. Currently, well-sampled ridges such
940 as the slow-spreading MAR are over-represented
941 in the global $^3He/^4He$ ratio database. The results
942 of this study suggest that at least the ambient
943 mantle beneath the ultra-slow spreading SWIR
944 has $^3He/^4He$ ratios of 6.3–7.3 R_a, which are sig-
945 nificantly lower than 8 ± 1 R_a. This conclusion is
946 supported by glass data near the BTJ, which also
947 indicate relatively low $^3He/^4He$ ratios [21].

5. Conclusions   948

949 The main results of this helium isotopic study
950 along the western SWIR include the following:
951 1. $^3He/^4He$ isotopic ratios are uniformly lower
952 than the putative MORB value (of 8 ± 1 R_a)
953 along both the oblique supersegment (9° to
954 16°E) and the orthogonal supersegment (16°
955 to 24°E) of the SWIR. $^3He/^4He$ ratios range
956 from 6.3 to 7.3 R_a. These low ratios show
957 that average values of $^3He/^4He$ for 'normal'
958 MORB ratios must be used carefully, and
959 may suggest that average $^3He/^4He$ ratios vary
960 from ridge to ridge. The low ratios are not the
961 result of post-eruptive radiogenic ingrowth
962 processes. The preferred explanation is intro-
963 duction of U+Th into the SWIR mantle source
964 by recycling of crustal or lithospheric material,
965 although detailed evaluation of this explana-
966 tion awaits further geochemical data from the
967 oblique and orthogonal supersegments. While
968 the He data set alone cannot support or refute
969 the existence of a veined mantle source for the
970 SWIR, a veined mantle source is consistent
971 with the different systematics of He, Nd, and
972 Sr isotopes throughout the study area.
973 2. Despite prediction by earlier studies of an in-
974 verse relationship between $^3He/^4He$ variability
975 and spreading rate, $^3He/^4He$ ratios between 10°
976 and 24°E are relatively constant, with a stan-
977 dard deviation from the mean of approxi-
978 mately 0.1–0.2 R_a.
979 3. Although the total variation in $^3He/^4He$ ratios
980 is relatively small, there is a systematic trend
981 along the orthogonal supersegment with $^3He/$

^{4}He ratios increasing from 6.6 to 7.3 R_a from west to east. Furthermore, ^{3}He/^{4}He is also significantly correlated with MBA along this trend. The glasses from the western end of the study area have significantly lower total ^{4}He concentrations than those from the east.

4. Despite a significant difference in ridge orientation between the orthogonal and oblique supersegments, there does not appear to be any systematic ^{3}He/^{4}He isotopic difference between the two ridge sections. Moreover, there is no evidence from ^{3}He/^{4}He data for influence of the high-^{3}He/^{4}He Bouvet plume on either supersegment.

References

[1] S.R. Hart, J.G. Schilling, J.L. Powell, Basalts from Iceland and along the Reykjanes Ridge: Strontium isotope geochemistry, Nature 246 (1973) 104–107.

[2] H.J.B. Dick, R.L. Fisher, W.B. Bryan, Mineralogic variability of the uppermost mantle along mid-ocean ridges, Earth Planet. Sci. Lett. 69 (1984) 88–106.

[3] J.-G. Schilling, Fluxes and excess temperatures of mantle plumes inferred from their interaction with migrating mid-ocean ridges, Nature 352 (1991) 397–403.

[4] G. Ito, J. Lin, Oceanic spreading center-hotspot interactions: Constraints from along-isochron bathymetric and gravity anomalies, Geology 23 (1995) 657–660.

[5] M.D. Kurz, W.J. Jenkins, J.G. Schilling, S.R. Hart, Helium isotopic variations in the mantle beneath the central North Atlantic Ocean, Earth Planet. Sci. Lett. 58 (1982) 1–14.

[6] R. Poreda, J.G. Schilling, H. Craig, Helium and hydrogen isotopes in ocean ridge basalts north and south of Iceland, Earth Planet. Sci. Lett. 78 (1985) 1–17.

[7] M. Moreira, T. Staudacher, P. Sarda, J.G. Schilling, C.J. Allègre, A primitive plume neon component in MORB: The Shona Ridge anomaly, South Atlantic (51-52 S), Earth Planet. Sci. Lett. 133 (1995) 367–377.

[8] D.W. Graham, K.T.M. Johnson, L.D. Prieve, J.E. Lupton, Hotspot-ridge interaction along the Southeast Indian Ridge near Amsterdam and St. Paul islands: helium isotope evidence, Earth Planet. Sci. Lett. 167 (1999) 297–310.

[9] M.D. Kurz, W.J. Jenkins, The distribution of helium in oceanic basalt glasses, Earth Planet. Sci. Lett. 53 (1981) 41–54.

[10] D.W. Graham, D.M. Christie, K.S. Harpp, J.E. Lupton, Mantle plume helium in submarine basalts from the Galapagos platform, Science 262 (1993) 2023–2026.

[11] R.J. Poreda, J.G. Schilling, Helium isotope ratios in Easter Microplate basalts, Earth Planet. Sci. Lett. 119 (1993) 319–329.

[12] D.L. Anderson, The statistics of helium isotopes along the global spreading ridge system and the central limit theorem, Geophys. Res. Lett. 27 (2000) 2401–2404.

[13] D.L. Anderson, A statistical test of the two reservoir model for helium isotopes, Earth Planet. Sci. Lett. 193 (2001) 77–82.

[14] M.D. Kurz, W.J. Jenkins, S.R. Hart, D.A. Clague, Helium isotopic variations in volcanic rocks from Loihi Seamount and the Island of Hawaii, Earth Planet. Sci. Lett. 66 (1983) 388–406.

[15] M.D. Kurz, D.P. Kammer, Isotopic evolution of Mauna Loa volcano, Earth Planet. Sci. Lett. 103 (1991) 257–269.

[16] M.D. Kurz, T.C. Kenna, J.C. Lassiter, D.J. DePaolo, Helium isotopic evolution of Mauna Kea volcano: first results from the 1-km drill core, J. Geophys. Res. 101 (1996) 11781–11791.

[17] D.R. Hilton, M.F. Thirwall, R.N. Taylor, B.J. Murton, A. Nichols, Controls on magmatic degassing along the Reykjanes Ridge with implications for the helium paradox, Earth Planet. Sci. Lett. 183 (2000) 43–50.

[18] M.D. Kurz, D. Geist, Dynamics of the Galapagos hotspot from helium isotope geochemistry, Geochim. Cosmochim. Acta 63 (1999) 4139–4156.

[19] D. Graham, J. Lupton, F. Albarede, M. Condomines, Extreme temporal homogeneity of helium isotopes at Piton la Fournaise, Reunion Island, Nature 347 (1990) 545–548.

[20] T. Staudacher, Ph. Sarda, C.J. Allègre, Noble gas systematics of Reunion Island, Indian Ocean, Chem. Geol. 89 (1990) 1–17.

[21] M.D. Kurz, A.P. le Roex, H.J.B. Dick, Isotope geochemistry of the oceanic mantle near the Bouvet triple junction, Geochim. Cosmochim. Acta 62 (1998) 841–852.

[22] D.W. Graham, S.E. Humphris, W.J. Jenkins, M.D. Kurz, Helium isotope geochemistry of some volcanic rocks from Saint Helena, Earth Planet. Sci. Lett. 110 (1992) 121–131.

[23] D.W. Graham, W.J. Jenkins, J.-G. Schilling, G. Thompson, M.D. Kurz, S.E. Humphris, Helium isotope geochemistry of mid-ocean ridge basalts from the South Atlantic, Earth Planet. Sci. Lett. 110 (1992) 133–147.

[24] S.R. Hart, A. Zindler, In search of a bulk-Earth composition, Chem. Geol. 57 (1986) 247–267.

[25] P. Sarda, M. Moreira, T. Staudacher, J.G. Schilling, C.J. Allègre, Rare gas systematics on the southernmost Mid-Atlantic Ridge: Constraints on the lower mantle and Dupal source, J. Geophys. Res. 105 (2000) 5973–5996.

[26] A.P. le Roex, H.J.B. Dick, R.T. Watkins, Petrogenesis of anomalous K-enriched MORB from the Southwest Indian Ridge: 11°53′E to 14°38′E, Contrib. Mineral. Petrol. 110 (1992) 253–268.

[27] R.A. Duncan, Hotspots in the southern oceans - an absolute frame of reference for motion of the Gondwana continents, Tectonophysics 74 (1981) 29–42.

[28] W.J. Morgan, Hotspot tracks and the early rifting of the Atlantic, Tectonophysics 94 (1982) 123–139.

[29] M. Ligi, E. Bonatti, G. Bortoluzzi, G. Carrara, P. Fabretti, D. Penitenti, D. Gilod, A.A. Peyve, S. Skolotnev, N. Turko, Death and transfiguration of a triple junction in the south Atlantic, Science 276 (1997) 243–245.

[30] J. Georgen, J. Lin, H.J.B. Dick, Evidence from gravity anomalies for interactions of the Marion and Bouvet hotspots with the Southwest Indian Ridge: Effects of transform offsets, Earth Planet. Sci. Lett. 187 (2001) 283–300.

[31] N.R. Grindlay, J. Madsen, C. Rommevaux-Jestin, J. Sclater, A different pattern of ridge segmentation and mantle Bouguer gravity anomalies along the ultra-slow spreading Southwest Indian Ridge (15°30′E to 25°E), Earth Planet. Sci. Lett. 161 (1998) 243–253.

[32] H.J.B. Dick, H. Schouten, J. Lin, Crustal accretion during extreme oblique spreading at an ultra-slow mid-ocean ridge, EOS Trans. AGU 82 (2001) S407.

[33] N.C. Mitchell, R.A. Livermore, Spiess Ridge: An axial high on the slow spreading Southwest Indian Ridge, J. Geophys. Res. 103 (1998) 15457–15471.

[34] A.P. le Roex, H.J.B. Dick, A.J. Erlank, A.M. Reid, F.A. Frey, S.R. Hart, Geochemistry, mineralogy and petrogenesis of lavas erupted along the Southwest Indian Ridge between the Bouvet Triple Junction and 11 degrees east, J. Petrol. 24 (1983) 267–318.

[35] J. Mahoney, A.P. le Roex, Z. Peng, R.L. Fisher, J.H. Natland, Southwestern limits of Indian Ocean ridge mantle and the origin of low $^{206}Pb/^{204}Pb$ mid-ocean ridge basalt: Isotope systematics of the central Southwest Indian Ridge (17°-50°E), J. Geophys. Res. 97 (1992) 19771–19790.

[36] J. Standish, H. Dick, A.P. le Roex, The influence of ridge geometry on mantle melting: Basalt geochemistry along the SWIR (9°-25°E), InterRidge South West Indian Ridge Workshop Abstracts Vol. 70, 2002.

[37] C.J. Allègre, M. Moreira, T. Staudacher, $^4He/^3He$ dispersion and mantle convection, Geophys. Res. Lett. 22 (1995) 2325–2328.

[38] H.J.B. Dick, J. Lin, H. Schouten, An investigation of the effects of ridge geometry on crustal accretion at ultra-slow spreading rates: The SW Indian Ridge from 9°-23.5°E, cruise report, R/V *Knorr* cruise 162, legs VII to IX (Dec. 9, 2000-Jan. 30, 2001), 2001.

[39] M.D. Kurz, J.J. Gurney, W.J. Jenkins, D.E. Lott, Helium isotopic variability from the Orapa Kimberlite, Earth Planet. Sci. Lett. 86 (1987) 57–68.

[40] K.L. Jochum, A.W. Hoffmann, E. Ito, H.M. Seufert, W.M. White, Potassium, uranium, and thorium in mid-ocean ridge basalt glasses and heat production, K/U, and K/Rb in the mantle, Nature 306 (1983) 431.

[41] D.W. Graham, W.J. Jenkins, M.D. Kurz, R. Batiza, Helium isotope disequilibrium and geochronology of glassy submarine basalts, Nature 326 (1987) 284–286.

[42] B.Y. Kuo, D.W. Forsyth, Gravity anomalies of the ridge-transform system in the South Atlantic between 31 and 34.5°S: Upwelling centers and variations in crustal thickness, Mar. Geophys. Res. 10 (1988) 205–232.

[43] J. Lin, G.M. Purdy, H. Schouten, J.-C. Sempere, C. Zervas, Evidence from gravity data for focused magmatic accretion along the Mid-Atlantic Ridge, Nature 344 (1990) 627–632.

[44] K. Breddam, M.D. Kurz, M. Storey, Mapping out the conduit of the Iceland mantle plume with helium isotopes, Earth Planet. Sci. Lett. 176 (2000) 45–55.

[45] D.W. Graham, J.E. Lupton, F.J. Spera, D.M. Christie, Upper-mantle dynamics revealed by helium isotope variations along the Southeast Indian Ridge, Nature 409 (2001) 701–703.

[46] F.G. Lemoine, S.C. Kenyon, J.K. Factor, R.G. Trimmer, N.K. Pavlis, D.S. Chinn, C.M. Cox, S.M. Klosko, S.B. Lutchke, M.H. Torrence, Y.M. Wang, R.G. Williamson, E.C. Pavlis, R.H. Rapp, T.R. Olson, The development of the Joint NASA GSFC and NIMI Geopotential Model EGM96, NASA Goddard Space Flight Center, Greenbelt, MD, 1998.

[47] C.H. Langmuir, Ryan, W.B.F., K. Lehnert, Y.J. Su, W. Jin, Petrological database of the ocean floor, http://petdb.ldeo.columbia.edu/petdb.

[48] W.H.F. Smith, D. Sandwell, Global sea floor topography from satellite altimetry and ship depth soundings, Science 277 (1997) 1956–1962.

[49] T.A. Minshull, N.J. Bruguier, J.M. Brozena, Ridge-plume interactions or mantle heterogeneity near Ascension Island?, Geology 26 (1998) 115–118.

[50] J. Douglass, J.G. Schilling, D. Fontignie, Plume-ridge interactions of the Discovery and Shona mantle plumes

1195 with the southern Mid-Atlantic Ridge (40°-55°S), J. Geo-
1196 phys. Res. 104 (1999) 2941–2962.

1197 [51] M.A. Richards, R.W. Griffiths, Thermal entrainment by
1198 deflected mantle plumes, Nature 342 (1989) 900–902.

1199 [52] R.M. Allen, G. Nolet, W.J. Morgan, K. Vogfjord, B.H.
1200 Bergsson, P. Erlendsson, G.R. Foulger, S. Jakobsdottir,
1201 B.R. Julian, M. Pritchard, S. Ragnarsson, R. Stefansson,
1202 Crustal thickness across Iceland, EOS Trans. AGU 78
1203 (1997) F500.

1204 [53] J. Lin, H.J.B. Dick, H. Schouten, J. Georgen, Evidence
1205 for off-axis volcanic relicts of the Bouvet hotspot and its
1206 interaction with the Southwest Indian Ridge, EOS Trans.
1207 AGU 82 (2001) F1169.

1208 [54] A.P. le Roex, H.J.B. Dick, A.M. Reid, F.A. Frey, A.J.
1209 Erlank, S.R. Hart, Petrology and geochemistry of basalts
1210 from the American-Antarctic Ridge, Southern Ocean: Im-
1211 plications for the westward influence of the Bouvet mantle
1212 plume, Contrib. Mineral. Petrol. 90 (1985) 367–380.

1213 [55] N.H. Sleep, Hotspots and mantle plumes: Some phenom-
1214 enology, J. Geophys. Res. 95 (1990) 6715–6736.

1215 [56] G. Ito, J. Lin, C.W. Gable, Dynamics of mantle flow and
1216 melting at a ridge-centered hotspot: Iceland and the Mid-
1217 Atlantic Ridge, Earth Planet. Sci. Lett. 144 (1996) 53–74.

1218 [57] N.M. Ribe, U.R. Christensen, The dynamics of plume-
1219 ridge interaction 2. Off-ridge plumes, J. Geophys. Res.
1220 101 (1996) 16195–16204.

1221 [58] G. Ito, J. Lin, C.W. Gable, Interaction of mantle plumes
1222 and migrating mid-ocean ridges: Implications for the Gal-
1223 apagos plume-ridge system, J. Geophys. Res. 102 (1997)
1224 15403–15417.

1225 [59] T.W. Trull, M.D. Kurz, Experimental measurements of
1226 ^{3}He and ^{4}He mobility in olivine and clinopyroxene at
1227 magmatic temperatures, Geochim. Cosmochim. Acta 57
1228 (1993) 1313–1324.

1229 [60] G.N. Hanson, Geochemical evolution of the suboceanic
1230 mantle, J. Geol. Soc. London 134 (1977) 1–19.

1231 [61] M.M. Hirschmann, E.M. Stolper, A possible role for gar-
1232 net pyroxenite in the origin of the 'garnet signature' in
1233 MORB, Contrib. Mineral. Petrol. 124 (1996) 185–208.

1234 [62] J. Georgen, J. Lin, H.J.B. Dick, Models of mantle upwell-
1235 ing beneath the Southwest Indian Ridge: The effects of
1236 ridge-transform geometry on magma supply at an ultra-
1237 slow spreading ridge, EOS Trans. AGU 79 (1998) F854.

1238 [63] H.J.B. Dick, J. Georgen, A.P. le Roex, J. Lin, J. Madsen,
1239 The influence of ridge geometry on mantle melting at an
1240 ultra-slow spreading ridge, EOS Trans. AGU 79 (1998)
1241 F919.

1242 [64] J.E. Lupton, D.W. Graham, J.R. Delaney, H.P. Johnson,
1243 Helium isotope variations in Juan de Fuca Ridge basalts,
1244 Geophys. Res. Lett. 20 (1993) 1851–1854.

1245 [65] E.M. Klein, C.H. Langmuir, H. Staudigal, Geochemistry
1246 of basalts from the South East Indian Ridge, 115°E-
1247 138°E, J. Geophys. Res. 96 (1991) 2089–2107.

1248 [66] B.P. West, W.S.D. Wilcock, J.-C. Sempéré, L. Géli,
1249 Three-dimensional structure of asthenospheric flow be-
1250 neath the Southeast Indian Ridge, J. Geophys. Res. 102
1251 (1997) 7783–7802.

1252 [67] C. Rommevaux-Jestin, C. Deplus, P. Patriat, Mantle Bou-
1253 guer anomaly along an ultra-slow spreading ridge: Impli-
1254 cations for accretionary processes and comparison with
1255 results from central Mid-Atlantic Ridge, Mar. Geophys.
1256 Res. 19 (1997) 481–503.

1257 [68] M. Cannat, C. Rommevaux-Jestin, D. Sauter, C. Deplus,
1258 V. Mendel, Formation of the axial relief at the very slow
1259 spreading Southwest Indian Ridge (49 degrees to 69 de-
1260 grees E), J. Geophys. Res. 104 (1999) 22825–22843.

1261 [69] J.J. Mahoney, J.H. Natland, W.M. White, R. Poreda,
1262 S.H. Bloomer, R.L. Fisher, A.N. Baxter, Isotopic and
1263 geochemical provinces of the western Indian Ocean
1264 spreading centers, J. Geophys. Res. 94 (1989) 4033–4052.

1265 [70] M. Moreira, M.D. Kurz, Subducted oceanic lithosphere
1266 and the origin of the 'himu' basalt helium isotopic signa-
1267 ture, Earth Planet. Sci. Lett. 189 (2001) 49–57.

1268 [71] C. DeMets, R.G. Gordon, D. Argus, S. Stein, Current
1269 plate motions, Geophys. J. Int. 101 (1990) 425–478.

1270 [72] C. DeMets, R.G. Gordon, D.F. Argus, S. Stein, Effect of
1271 recent revisions to the geomagnetic reversal time scale on
1272 estimates of current plate motions, Geophys. Res. Lett. 21
1273 (1994) 2191–2194.